



Cite this: DOI: 10.1039/d3tc00768e

Luminescent Pb-free perovskites: low-cytotoxicity materials for primary thermal sensing†

Luan N. Passini,^a Fernando E. Maturi,^{b,c} Roberta S. Pugina,^d Eloísa G. Hilário,^d Marina Fontes,^e Hernane S. Barud,^e Luís D. Carlos,^b José Mauricio A. Caiut^b and Danilo Manzani^{b,*}

Selecting a suitable host matrix to perform temperature sensing in biomedical applications requires low cytotoxicity, facile synthesis, and an ability to be doped with light-emitting ions. With this perspective, indium-based halide double perovskites, specifically $\text{Cs}_2\text{AgIn}_{0.9}\text{Bi}_{0.1}\text{Cl}_6$, $\text{Cs}_2\text{Ag}_{0.6}\text{Na}_{0.4}\text{InCl}_6$, and $\text{Cs}_2\text{Ag}_{0.6}\text{Na}_{0.4}\text{In}_{0.9}\text{Bi}_{0.1}\text{Cl}_6$, were chosen as host materials to develop lanthanide-based primary thermometers due to their low phonon energy and ease of synthesis. The incorporation of Na^+ and Bi^{3+} into the perovskite cubic crystal lattice was confirmed by X-ray diffraction and Raman spectroscopy while the optical properties of both the undoped and $\text{Yb}^{3+}/\text{Er}^{3+}$ co-doped perovskites were assessed by diffuse reflectance and photoluminescence spectroscopies. The obtained perovskite samples demonstrated excellent thermal stability, with the ability to withstand temperatures as high as 500 °C. A temperature-dependent green emission of Er^{3+} was observed in the co-doped samples upon 980 nm irradiation, yielding a relative thermal sensitivity and uncertainty in temperature values of 1.3% K^{-1} and 0.3 K, respectively. Incorporating the obtained perovskites (0.05 to 0.20 mg mL^{-1}) into L2929 cells as an *in vitro* model resulted in high cell viability, underscoring the benefits of selecting such a low-cytotoxicity material for applications in biological media.

Received 3rd March 2023,

Accepted 9th May 2023

DOI: 10.1039/d3tc00768e

rsc.li/materials-c

1. Introduction

Lead halide perovskites (LHPs) have attracted significant attention in recent years due to their outstanding optical properties, including high absorption coefficients, low exciton binding energies, high charge-carrier mobilities, and low trap densities.^{1–3} These remarkable properties are a result of the conventional ABX_3 structure of the LHPs, which enables the bandgap energy to be fine-tuned by modifying the elements in the A, B, and/or X sites. Typically, the A-site is a monovalent cation, such as Cs^+ , CH_3NH_3^+ , or $\text{CH}(\text{NH}_2)_2^+$, while the B-site corresponds to a divalent cation (Pb^{2+}), and the X-site is commonly occupied by halides, such as Cl^- , Br^- , or I^- .^{1,4}

However, the high solubility of lead in water limits the commercial applications of LHPs on a larger scale due to environmental and health concerns.^{5–7}

Lead-free double perovskites ($\text{A}_2\text{B}'\text{B}''\text{X}_6$) have emerged as a promising alternative to LHPs because they are environmentally friendly and chemically stable while being able to absorb light across the visible spectral range.⁸ In particular, indium (In)-based double halide perovskites exhibit a cubic crystal structure with a direct bandgap between the visible (Vis) and ultraviolet (UV) spectral regions, presenting higher photoluminescence quantum efficiencies in comparison with the indirect bandgap double perovskites.^{9–11} However, the parity-forbidden transition is a major drawback when dealing with In-based perovskites for luminescent applications. To address this issue, the incorporation of Bi^{3+} and/or Na^+ has been used to break the parity-forbidden transition feature while preserving the direct bandgap transitions.^{11–14}

Additionally, In-based perovskite materials present low phonon energy and are excellent candidates for doping with luminescent trivalent lanthanide ions (Ln^{3+}).^{15,16} Ln^{3+} -doped luminescent materials are versatile, chemically stable, and show narrow emission bands (<10 nm) covering the UV, Vis, and near-infrared (NIR) spectral ranges, with high Vis emission quantum yields.^{17,18} Moreover, their applications for *in vivo* thermal imaging¹⁹ and early tumor detection^{20–23} have been

^a São Carlos Institute of Chemistry, University of São Paulo (USP), São Carlos, SP, 13560-970, Brazil. E-mail: dmanzani@usp.br

^b Phantom-g, CICECO-Aveiro Institute of Materials, Department of Physics, University of Aveiro, Aveiro, 3810-193, Portugal

^c Institute of Chemistry, São Paulo State University (UNESP), Araraquara, SP, 14800-060, Brazil

^d Department of Chemistry, Faculty of Philosophy, Sciences and Letters, University of São Paulo (USP), Ribeirão Preto, SP, 14040-901, Brazil

^e BioPolMat-Biopolymers and Biomaterials Research Group, University of Araraquara (UNIARA), Araraquara, SP, 14801-040, Brazil

† Electronic supplementary information (ESI) available. See DOI: <https://doi.org/10.1039/d3tc00768e>

garnering great interest in recent years due to their ability to perform excitation and emission in the biological spectral window where the absorption and scattering of light in biological tissues are reduced.^{17,24} Some Ln^{3+} ions also display a strong temperature-dependent luminescence, such as Pr^{3+} ,²⁵ Nd^{3+} ,²⁶ Eu^{3+} ,²⁷ Ho^{3+} ,²⁸ Tm^{3+} ,²⁹ and Er^{3+} ,^{30–32} making them excellent candidates for thermal sensing, covering intervals from the cryogenic (<100 K) to physiological (298–323 K) temperatures.

Er^{3+} -doped materials are interesting due to their well-established narrow emission bands and long-lived excited states.³³ The $^2\text{H}_{11/2}$ and $^4\text{S}_{3/2}$ emitting levels of Er^{3+} are particularly attractive because they are so close in energy ($\sim 750\text{ cm}^{-1}$) that even small temperature variations can change the relative population between them. Although the behavior of these so-called thermally coupled levels can be described by using the Maxwell–Boltzmann statistics,¹⁷ Balabhadra *et al.* reported an ingenious approach to predict the absolute temperature (T) using a thermometric parameter (Δ) based on the luminescence intensity ratio (LIR) between the integrated intensities of the emission bands corresponding to the $^2\text{H}_{11/2} \rightarrow ^4\text{I}_{15/2}$ (I_{H}) and $^4\text{S}_{3/2} \rightarrow ^4\text{I}_{15/2}$ (I_{S}) transitions of Er^{3+} ($\Delta = I_{\text{H}}/I_{\text{S}}$):³²

$$\frac{1}{T} = \frac{1}{T_0} - \frac{k_{\text{B}}}{\Delta E} \ln\left(\frac{\Delta}{\Delta_0}\right) \quad (1)$$

where T_0 is the room temperature, k_{B} is the Boltzmann constant, Δ_0 is the value of Δ at T_0 (LIR in the absence of laser-induced heating), and ΔE is the energy gap between the $^2\text{H}_{11/2}$ and $^4\text{S}_{3/2}$ emitting levels, which is calculated from the difference between the barycenters of the $^2\text{H}_{11/2} \rightarrow ^4\text{I}_{15/2}$ and $^4\text{S}_{3/2} \rightarrow ^4\text{I}_{15/2}$ emission bands. This method provides a primary thermometric approach for measuring the absolute temperature that relies solely on the emission of the thermally-coupled levels of Er^{3+} regardless of the medium, whereby thermal readouts can be performed based on a well-established equation of state without needing external calibration.³⁴

While several primary luminescent thermometers have been reported, such as semiconductor nanoparticles,³⁵ organic–inorganic hybrids,³⁶ Ln^{3+} luminescent complexes,^{37,38} and Ln^{3+} luminescent nanoparticles,^{39,40} Er^{3+} -based LIR primary thermometers are preferred because they require simple instrumentation and are not affected by the local intensity variation (*e.g.*, emitting centers concentration and/or excitation source oscillation),¹⁸ paving the way for developing new reliable thermal sensors without the need for recording time-consuming calibration curves. Furthermore, Suta *et al.* recently suggested that Er^{3+} is the best Ln^{3+} to perform temperature sensing around the room temperature range,⁴¹ with the added benefit of it being able to operate in the biological spectral window when co-doped with Yb^{3+} , where the excitation at 980 nm is safer for tissues in biological applications due to the lower absorption in the NIR.⁴²

For this reason, we herein report the structural and optical characterization of novel low-cytotoxicity $\text{Er}^{3+}/\text{Yb}^{3+}$ co-doped In-based perovskite materials synthesized *via* a simple

wet-chemical route, which were then used to predict temperature based on the primary luminescent thermometric ability of Er^{3+} emission in the green spectral range upon Yb^{3+} excitation in the NIR. To the best of our knowledge, this is the first report demonstrating lead-free double halide perovskites working as primary thermometers.

2. Results and discussion

2.1. Structural, optical, thermal, and cytotoxic evaluations

The proposed wet-chemical route used to obtain the In-based perovskites allowed for the synthesis of pure and crystalline samples (see Experimental Section for the detailed compositions and labels), displaying sharp and well-defined diffraction peaks, as shown in Fig. 1. The X-ray diffraction (XRD) results revealed that the In-based perovskites exhibited a cubic crystal system corresponding to the $Fm\bar{3}m$ space group with lattice parameters of 10.48 Å for a , b , and c , and a cell volume of 1151.21 Å³, characteristic of CsAgInCl_6 perovskites.⁴³ However, the addition of bismuth led to an increase in the lattice and cell volume as the larger Bi^{3+} radius of 1.03 Å in comparison to In^{3+} (0.80 Å) affected the assembly of the crystal structure. The diffractograms of the obtained samples presented in Fig. 1 display the characteristic peaks assigned to the (200), (220), (222), (400), (422), (440), (620), and (622) diffraction planes associated with In-based perovskites.⁴⁴ The synthesized perovskites showed good agreement with the standard powder XRD pattern taken from the Inorganic Crystal Structure Database (ICSD) number 11524 corresponding to $\text{Cs}_2\text{AgInCl}_6$, especially the sample $\text{pIn}_{0.9}$. Nevertheless, $\text{pAg}_{0.6}\text{In}$ and $\text{pAg}_{0.6}\text{In}_{0.9}$ showed more intense (200) and (222) peaks compared to the $\text{pIn}_{0.9}$ sample due to the incorporation of Na^+ in the Ag^+ site.⁴⁵

The $\text{Yb}^{3+}/\text{Er}^{3+}$ co-doped In-based perovskites also gave rise to a crystalline cubic phase with similar diffraction patterns (Fig. 1a–c), although some differences must be highlighted. For instance, the $\text{pAg}_{0.6}\text{In}$ sample displayed a clear distinction between the intensity of the (222) and (400) planes for each dopant concentration. This intensity change was likely due to the concentration and dopant chemical nature, such as its ionic radius. It is expected that the replacement of In^{3+} (0.80 Å) in the perovskite lattice by Yb^{3+} (0.89 Å) and Er^{3+} (0.87 Å) when doping with Ln^{3+} would lead to an expansion of the crystal lattice. Moreover, in the Ln^{3+} co-doped samples, the diffraction peaks shifted to lower 2θ angles due to the lanthanide incorporation in the lattice. However, there were no significant structural modifications observed when In-based perovskites were doped with Ln^{3+} , probably due to the similarity of the ionic radii of Ln^{3+} and In^{3+} . The morphology of the samples was evaluated by scanning electron microscopy (SEM), which revealed that the samples were obtained with an irregular octahedral shape between 10–20 μm , as shown in Fig. S1 (ESI†).

Fig. 2 presents the Raman spectra of all the synthesized In-based perovskites, revealing up to six vibrational modes below 400 cm^{-1} . The Raman bands centered at 48, 110, 139, 169, 239, and 297 cm^{-1} corresponded to the $\text{T}_{2g}(\text{L})$, $\text{T}_{2g}(\text{Bi}^{3+})$, $\text{T}_{2g}(\text{In}^{3+})$,

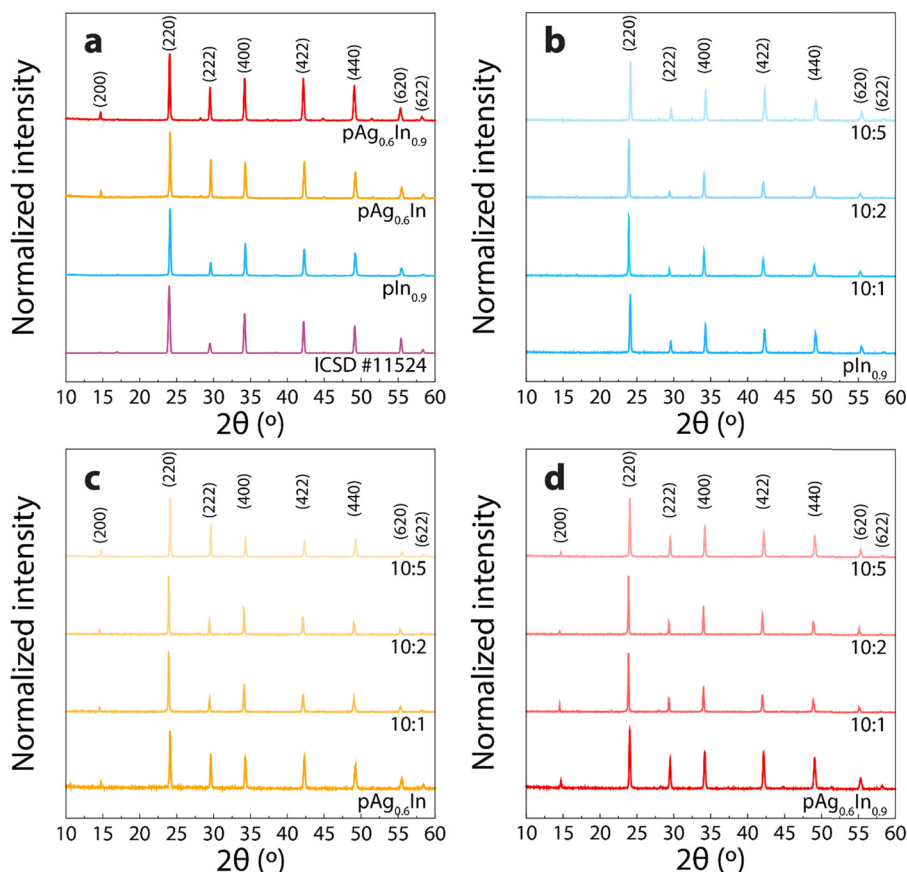


Fig. 1 (a) X-Ray diffractograms of the obtained powders for the $\text{pIn}_{0.9}$, $\text{pAg}_{0.6}\text{In}$, and $\text{pAg}_{0.6}\text{In}_{0.9}$ undoped perovskite hosts. XRD of the corresponding $\text{Yb}^{3+}/\text{Er}^{3+}$ co-doped In-based perovskites (b) $\text{pIn}_{0.9}$, (c) $\text{pAg}_{0.6}\text{In}$, and (d) $\text{pAg}_{0.6}\text{In}_{0.9}$ with $\text{Yb}^{3+}:\text{Er}^{3+}$ ratios of 10 : 1, 10 : 2, and 10 : 5, respectively.

$E_g(\text{In}^{3+})$, $E_g(\text{Bi}^{3+})$, and A_{1g} vibrational modes in sample $\text{pAg}_{0.6}\text{In}_{0.9}$, respectively, in excellent agreement with the previously reported values.^{43,46} The T_{2g} , E_g , and A_{1g} vibrational modes originated from AgCl_6 , InCl_6 , and BiCl_6 octahedrons, respectively, in which the $T_{2g}(\text{Bi}^{3+})$ and $E_g(\text{Bi}^{3+})$ vibrational modes from the Bi^{3+} -containing samples were assigned to Bi-Cl stretching. It is noteworthy that the sample $\text{pAg}_{0.6}\text{In}_{0.9}$ exhibited a greater number of Raman bands compared to the other samples due to the contribution of all the mixed elements, as observed in the XRD results. Moreover, the phonon energy of the In-based perovskites, as indicated by the band peaking around 297 cm^{-1} in all the Raman spectra, was lower than the values reported for host materials commonly used for doping with lanthanide ions (see Table 1 for the reference values). This suggests that the obtained samples are highly suitable for enhancing the optical properties of Er^{3+} and Yb^{3+} in

upconverting applications. Furthermore, it is important to highlight that all the Raman spectra of the $\text{Yb}^{3+}/\text{Er}^{3+}$ co-doped samples presented identical band shapes and positions compared to the host matrices.

Incorporating Bi^{3+} into an In-based perovskite lattice has been found to change its optical properties, as noted by Siddique *et al.*⁴³ This is due to the distortion of the octahedron in the perovskite crystal structure caused by Bi-alloying, leading to an increase in the In-Cl bond length and a decrease in the Bi-Cl bond length, resulting in self-trapped excitons (STEs) originating from the structural distortion caused by the Bi^{3+} incorporation. This explains the bright luminescence of Bi^{3+} -doped In-based perovskites.⁴³ In other words, incorporating a certain amount of Bi^{3+} can maintain the direct bandgap of $\text{Cs}_2\text{AgInCl}_6$ and break the parity-forbidden transition issue.

The energy bandgap values (E_g) for all the perovskite host matrices were obtained from UV-Vis diffuse reflectance analysis by applying the Tauc plot method.⁵⁰ Thus, by manipulating the recorded data utilizing the Kubelka-Munk function $\alpha = (1 - R)^2/2R$, where α is the optical absorption coefficient and R is the reflectance, it was possible to obtain the values of E_g by extrapolating the linear fit (Tauc plot) to the x -axis. Fig. 3 and Table 2 display the energy graphs and bandgap values obtained for all the In-based perovskites matrices.

Table 1 Phonon energies of different host matrices used for lanthanide-doping

Host	Phonon energy (cm^{-1})	Ref.
$\text{pIn}_{0.9}$, $\text{pAg}_{0.6}\text{In}$, and $\text{pAg}_{0.6}\text{In}_{0.9}$	297	This work
$\beta\text{-NaYF}_4$	350	47
Y_2O_3	380	48
YOF	400	49

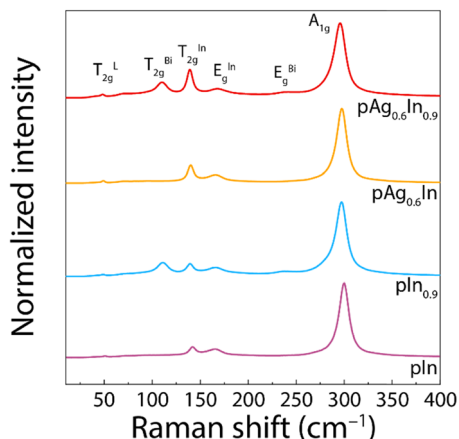


Fig. 2 Raman spectra of the different In-based perovskites.

From the reflectance spectra, two E_g values were extracted from the samples (Fig. 3), which were assigned to the material energy bandgap and to the surface/defect states, which were in excellent agreement with those presented in the literature.⁵¹ These two values of E_g for $\text{pIn}_{0.9}$ and $\text{pAg}_{0.6}\text{In}_{0.9}$ perovskites might be related to the energy gap of the material (higher eV), and the surface/defect states (lower eV), as aforementioned in the discussion of the Raman results. The formation of these vacancies/defect states was associated with the addition of Bi^{3+} in the perovskite lattice, since both perovskite samples containing Bi^{3+} showed the same behavior. The incorporation of Er^{3+} and Yb^{3+} into the In-based perovskites' lattice did not significantly change the values of the energy gap. The calculated E_g for the Ln^{3+} -doped samples is presented in Table S1 (ESI†). It is worth pointing out that the incorporation of Bi^{3+} led to lower phonon energies, as seen in Fig. 2. Therefore, the lower E_g of 3.06 and 2.96 eV for $\text{pIn}_{0.9}$ and $\text{pAg}_{0.6}\text{In}_{0.9}$, respectively, may be attributed to the formation of STEs.^{51–54}

The obtained perovskite samples presented excellent thermal stability, in addition to high crystallinity, low phonon energy, and direct bandgap properties. The thermogravimetric curves in Fig. 4a demonstrate that the samples could withstand temperatures as high as 500 °C. This remarkable thermal stability is a desirable characteristic for perovskite materials and makes them suitable for high-temperature applications.

Table 2 Calculated energy bandgaps of the undoped In-based perovskites

Sample	E_{g1} (± 0.03 eV)	E_{g2} (± 0.03 eV)
$\text{pIn}_{0.9}$	3.48	3.06
$\text{pAg}_{0.6}\text{In}$	3.69	—
$\text{pAg}_{0.6}\text{In}_{0.9}$	3.60	2.96

Additionally, the metabolic viability of the synthesized perovskite samples was assessed using the MTT assay 48 h after exposure to determine their cytotoxicity (Fig. 4b). Here, concentrations of 0.05, 0.10, and 0.20 mg mL^{-1} were deemed safe for all the perovskites, with cell viability exceeding 70%. According to ISO 10993-5, a reduction of cell viability greater than 30% is considered cytotoxic.⁴⁶ Thus, perovskite concentrations ranging from 0.05 to 0.20 mg mL^{-1} exhibit high potential for biomedical applications. More detailed biological tests were not performed. The obtained results are encouraging for further works using perovskite NCs aiming for more detailed findings for assessing their application in the medical field.

2.2. Photoluminescent properties of the In-based perovskites

Fig. 5 presents the excitation spectra of the undoped perovskite samples. The In-based perovskite matrices presented a high-intensity excitation band when the emission band peak around 610 nm was monitored. The $\text{pIn}_{0.9}$ and $\text{pAg}_{0.6}\text{In}$ samples showed a great difference between the excitation spectra in terms of the shape and band position arising from the incorporation of Bi^{3+} and Na^{+} into the host matrix. The excitation spectrum of the $\text{pAg}_{0.6}\text{In}_{0.9}$ sample showed a shape and band position that resembled a mixture of the previous ones, as a result of the presence of both ions. For the excitation spectra, the most intense regions were centered at 355 nm and 394 nm for $\text{pIn}_{0.9}$, 360 nm for $\text{pAg}_{0.6}\text{In}$, and 360 nm for the $\text{pAg}_{0.6}\text{In}_{0.9}$ sample. Therefore, when excitation occurs at these maximum bands, the sample is excited at the intrinsic bandgap (lower wavelengths) and the surface/defect states (higher wavelengths).⁵² The emission spectra shown in Fig. 5d, e and f reveal that all the samples presented a broad emission band from 450 to 800 nm. Samples $\text{pIn}_{0.9}$ and $\text{pAg}_{0.6}\text{In}_{0.9}$, in which In^{3+} was mixed with Bi^{3+} , showed an intense and bright

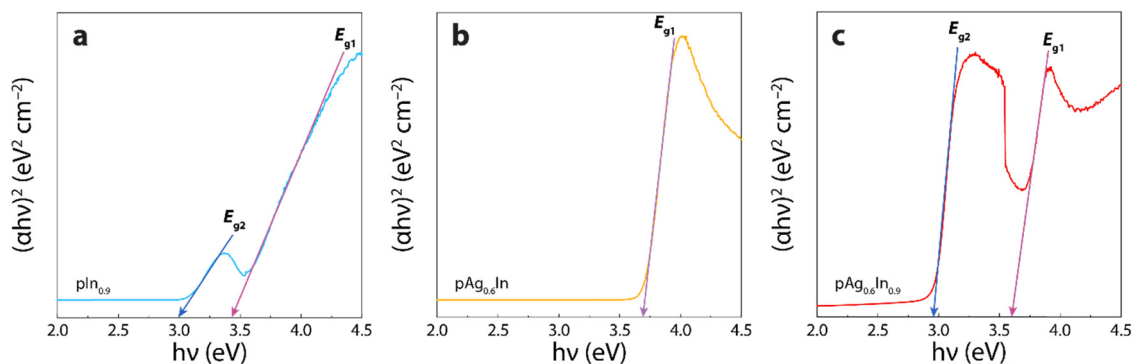


Fig. 3 Tauc plots of the energy bandgap (E_g) determination for the undoped (a) $\text{pIn}_{0.9}$, (b) $\text{pAg}_{0.6}$, and (c) $\text{pAg}_{0.6}\text{In}_{0.9}$ perovskite samples.

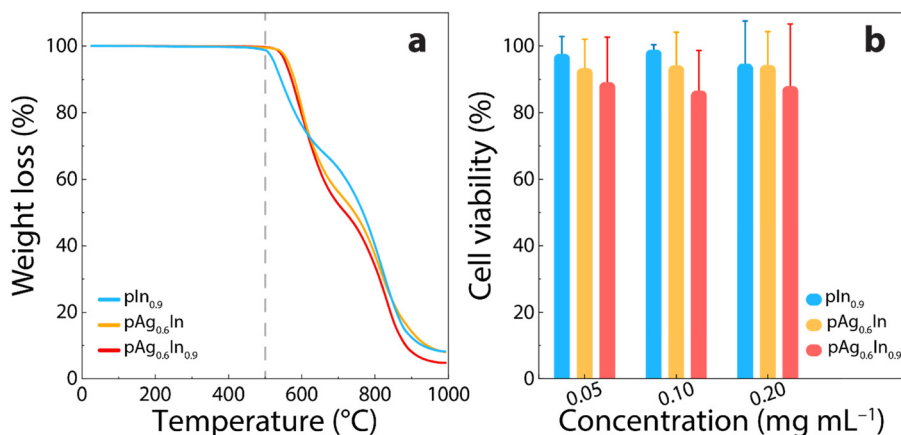


Fig. 4 (a) Thermograms of the undoped perovskite samples highlighting their thermal stability. (b) Cell viability (percentual values) as a function of the undoped perovskites' concentration assessed by the MTT assay. Each value corresponds to the mean \pm standard deviation.

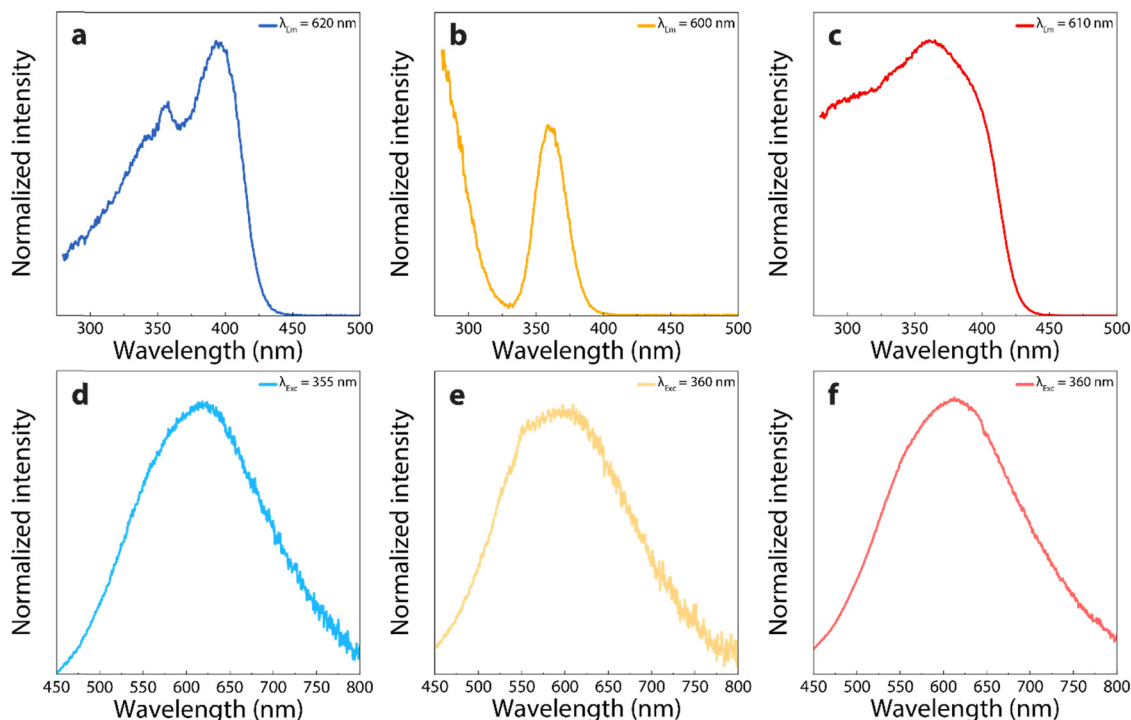


Fig. 5 Excitation spectra of the (a) pIn_{0.9}, (b) pAg_{0.6}In, and (c) pAg_{0.6}In_{0.9} In-based perovskite matrices when monitoring the emission at 620, 600, and 610 nm, respectively. Emission spectra of the (d) pIn_{0.9}, (e) pAg_{0.6}In, and (f) pAg_{0.6}In_{0.9} In-based perovskite matrices under excitation at 355, 360, and 360 nm, respectively.

yellowish white luminescence that could be perceived by the naked eye, as shown in Fig. S2 (ESI[†]).⁵¹

The co-doped In-based perovskite samples presented a downshifting emission band centered at 1540 nm, attributed to the characteristic $^4I_{13/2} \rightarrow ^4I_{15/2}$ transition of Er³⁺ in the NIR,⁵³ which was observed under excitation of the perovskite host matrix (UV) or directly with Er³⁺ (522 nm), indicating an energy transfer from the In-based perovskite matrix to Er³⁺, where the latter case resulted in a higher emission intensity. Despite the energy transfer from the In-based perovskite to the

lanthanide ion, no emission was observed in the visible spectral range, possibly due to the strong broadband emission of the In-based perovskite (Fig. 5). The excitation and emission spectra of the Yb³⁺/Er³⁺ co-doped samples are presented in Fig. S2 (ESI[†]). Moreover, the co-doped samples also displayed an upconverting emission of Er³⁺ upon 980 nm continuous-wave (CW) irradiation, as shown in Fig. 6.

The upconverting emission spectra of the pIn_{0.9}:Yb³⁺/Er³⁺ (10:5) sample exhibited the characteristic emission bands of Er³⁺ related to the $^2H_{11/2} \rightarrow ^4I_{15/2}$ (510–541 nm) and $^4S_{3/2} \rightarrow ^4I_{15/2}$

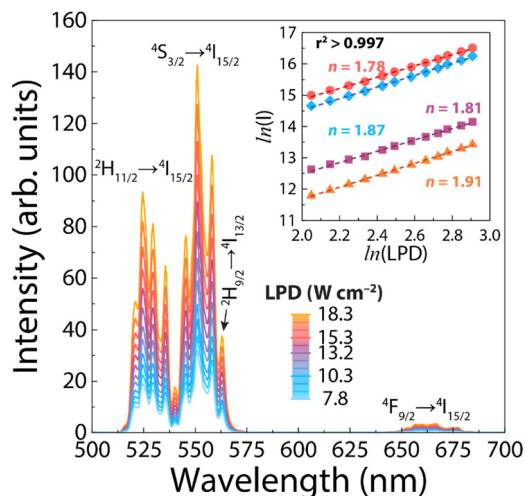


Fig. 6 Upconverting emission spectra under excitation at 980 nm of the $\text{pIn}_{0.9}$ sample co-doped with $\text{Yb}^{3+}/\text{Er}^{3+}$ (10:5), when varying the laser power density (LPD) from 7.8 to 18.3 W cm^{-2} . The inset displays the double-logarithmic plot of the integrated emission against the LPD. The data in red, blue, purple, and orange correspond to the estimation of the number of photons (n) involved in the upconversion mechanism of the transitions $4\text{S}_{3/2} \rightarrow 4\text{I}_{15/2}$, $2\text{H}_{11/2} \rightarrow 4\text{I}_{15/2}$, $2\text{H}_{9/2} \rightarrow 4\text{I}_{13/2}$, and $4\text{F}_{9/2} \rightarrow 4\text{I}_{15/2}$, respectively, with $r^2 > 0.997$ for all the fits.

(541–561 nm) transitions in the green spectral region and the $4\text{F}_{9/2} \rightarrow 4\text{I}_{15/2}$ (635–690 nm) transition in the red spectral region. Moreover, a shoulder around 562 nm could be observed, corresponding to the $2\text{H}_{9/2} \rightarrow 4\text{I}_{13/2}$ transition originating from the upper $2\text{H}_{9/2}$ energy level of Er^{3+} due to the low phonon energy of the perovskite host matrix.^{18,55,56} The energy transfer upconversion (ETU, 10^{-3}) process is more efficient than excited-state absorption (ESA, 10^{-5}), and was likely responsible for the upconverting emission in the co-doped In-based, although the ESA process could also have contributed.^{57,58} Furthermore, it is worth pointing out that the integrated intensity (I) of the emission bands assigned to the above-mentioned transitions of Er^{3+} increased upon increasing the power of the 980 nm excitation source, following the power law $I \propto \text{LPD}^n$, where, n is the number of photons involved in the upconversion mechanism and can be retrieved from the slope of I versus LPD in a double-logarithmic plot, as shown in the inset of Fig. 6.⁵⁹ The values of n were 1.85, 1.76, 1.79, and 1.90 for the $2\text{H}_{11/2} \rightarrow 4\text{I}_{15/2}$, $4\text{S}_{3/2} \rightarrow 4\text{I}_{15/2}$, $2\text{H}_{9/2} \rightarrow 4\text{I}_{13/2}$, and $4\text{F}_{9/2} \rightarrow 4\text{I}_{15/2}$ transitions, respectively, indicating that two photons were involved in the upconversion emission of the perovskite samples. The upconverting emission spectra of $\text{Yb}^{3+}/\text{Er}^{3+}$ co-doped $\text{pIn}_{0.9}$, $\text{pAg}_{0.6}\text{In}$, and $\text{pAg}_{0.6}\text{In}_{0.9}$ samples at 10:1, 10:2, and 10:5 ratios under varying LPD, respectively, are displayed in Fig. S3 (ESI[†]).

2.3. Primary thermometry on the luminescent In-based perovskites

We took advantage of the low-cytotoxicity of the obtained In-based perovskites co-doped with $\text{Yb}^{3+}/\text{Er}^{3+}$ to assess their thermal sensing ability by applying the primary thermometric

approach described by eqn (1) using the temperature-dependent emission spectra of the $\text{pAg}_{0.6}\text{In}_{0.9}:\text{Yb}^{3+}/\text{Er}^{3+}$ (10:2) sample, as shown in Fig. 7. The results indicated that upon increasing the temperature, I_{H} and I_{S} presented a steep and gentle increase, respectively, due to the thermal redistribution between the $2\text{H}_{11/2}$ and $4\text{S}_{3/2}$ emitting levels. Replacing the values of ΔE ($753 \pm 10 \text{ cm}^{-1}$), T_0 ($293.5 \pm 0.1 \text{ K}$), Δ_0 (0.4283 ± 0.0007), and the experimental values of Δ obtained from the temperature-dependent emission spectra from sample $\text{pAg}_{0.6}\text{In}_{0.9}:\text{Yb}^{3+}/\text{Er}^{3+}$ (10:2) in eqn (1) resulted in an excellent agreement between the measured and calculated temperatures, thus validating the primary thermal sensing ability of the obtained sample.

Once the same approach can be applied to the different In-based perovskite samples, it is possible to use the relative thermal sensitivity, $S_r = \frac{1}{\Delta} \left| \frac{\partial \Delta}{\partial T} \right| = \frac{\Delta E}{k_B T^2}$, which gives the relative change of Δ with respect to the temperature, and the uncertainty in temperature, $\delta T = \frac{\delta \Delta / \Delta}{S_r}$, which represents the smallest temperature resolvable by the thermometer.¹⁷ This enables a comparison of the thermometric performance of the obtained samples with different Er^{3+} -based luminescent thermometers, regardless of their particle size or chemical surface functionalization, as presented in Table 3. The thermal evolution of S_r and δT for the temperature range studied in this work are displayed in Fig. S4 (ESI[†]).

The calculated values of the energy gap were similar for all the obtained samples, therefore, the values of S_m and δT were essentially the same. As S_r is proportional to ΔE , the S_m and δT values are in good agreement with those reported in the literature for Er^{3+} -based primary thermometers (Table 3), which usually lie in the 1.0–1.3% K^{-1} and 0.1–0.9 K ranges, respectively, indicating that the In-based perovskite samples are indeed excellent primary luminescent thermometers for performing thermal readouts regardless of their composition. In this sense, the low cytotoxicity, outstanding optical properties, and reliable thermal sensing ability pave the way for using In-based perovskites for applications in solar energy conversion and *in vitro/in vivo* thermometry.

3. Conclusion

In this study, we demonstrated the potential of In-based double halide perovskites as luminescent thermometers for potential use in biomedical applications. The synthesis of highly crystalline perovskites with low cytotoxicity was achieved through a facile wet-chemical route, and the incorporation of Na^+ and Bi^{3+} into the perovskites' crystal lattice was confirmed by XRD and Raman spectroscopy. The optical properties of both the undoped and Ln^{3+} -doped perovskites were characterized, whereby the incorporation of $\text{Yb}^{3+}/\text{Er}^{3+}$ ions in the perovskites resulted in upconversion luminescence, which was used to develop primary thermometers with a high relative thermal sensitivity of 1.3% K^{-1} and uncertainty in temperature values

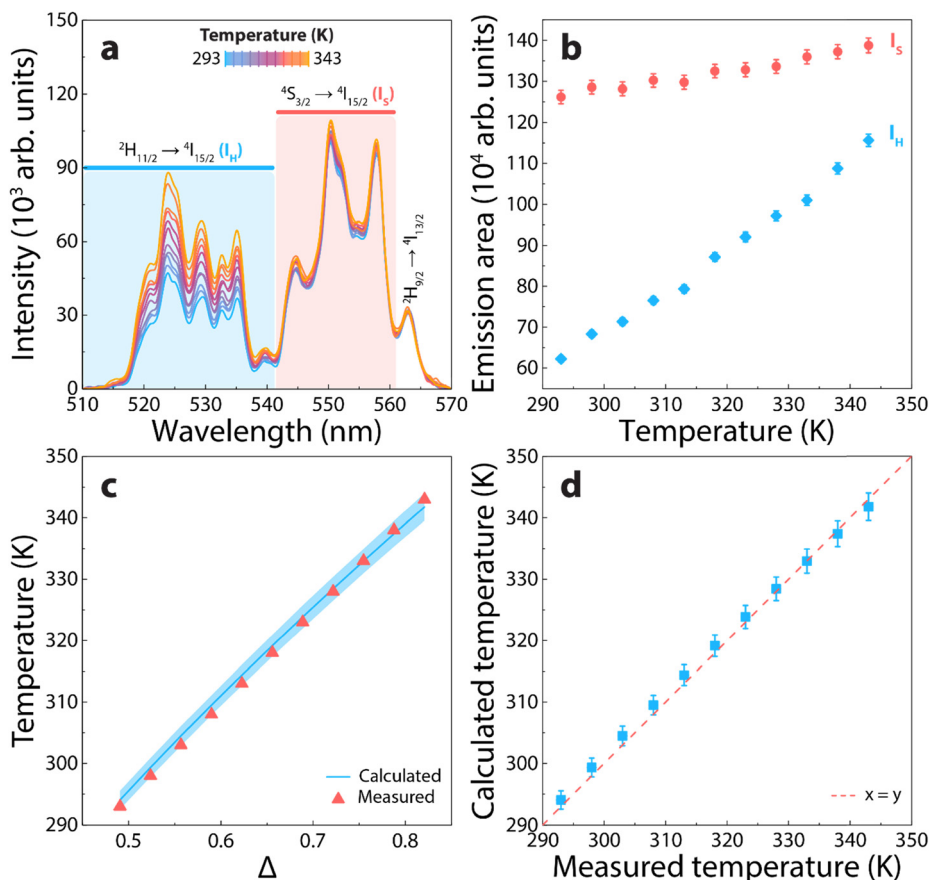


Fig. 7 (a) Temperature-dependent emission spectra of the $\text{pAg}_{0.6}\text{In}_{0.9}:\text{Yb}^{3+}/\text{Er}^{3+}$ (10:2) sample under laser excitation at 980 nm ($\text{LPD} = 18.3 \text{ W cm}^{-2}$). (b) Thermal evolution of the integrated emission areas of the $^2\text{H}_{11/2} \rightarrow ^4\text{I}_{15/2}$ (I_{H}) and $^4\text{S}_{3/2} \rightarrow ^4\text{I}_{15/2}$ (I_{S}) transitions. (c) Temperature dependence of the experimental Δ values. The solid blue line presents the values of temperature calculated through eqn (1) and the shadowed area displays their corresponding uncertainties obtained from propagating the uncertainties of eqn (1). The triangles in red display the values of temperature measured with a K-type thermocouple. (d) Correlation between the temperature measured with the thermocouple (x-axis) and the temperature calculated with eqn (1) (y-axis). The dashed red line is a guide for the eyes corresponding to $x = y$.

as low as 0.3 K, which were in good agreement with previously reported values. Furthermore, the excellent thermal stability of the perovskites was demonstrated, with the samples remaining stable at up to 500 °C. The biocompatibility of the perovskites was also evaluated, showing high cell viability in L929 cells, indicating their potential for use in targeted bioimaging and the real-time monitoring of cancer cells. These findings pave the way for using In-based perovskites in biomedical applications, as well as in solar energy conversion.

4. Experimental section

Materials

Hydrochloric acid (HCl, Sigma-Aldrich, 37%), cesium chloride (CsCl, Vetec, P.A.), silver chloride (AgCl, Sigma-Aldrich, 99%), bismuth chloride (BiCl_3 , Sigma-Aldrich, $\geq 98\%$), sodium chloride (NaCl, Synth, P.A. A.C.S.), indium oxide (In_2O_3 , Merck, 99%), erbium oxide (Er_2O_3 , Sigma-Aldrich, 99.9%), ytterbium oxide (Yb_2O_3 , Lumitech, 99.99%), and isopropyl alcohol (Exodo, 99.5%) were purchased and used as received.

Synthesis of the In-based double halide perovskites

In-based double halide perovskites were prepared according to the modified synthesis procedure reported by Kumar Chini *et al.*⁶⁴ First, the undoped perovskites with compositions listed in Table 4 and labeled as $\text{pIn}_{0.9}$, $\text{pAg}_{0.6}\text{In}$, and $\text{pAg}_{0.6}\text{In}_{0.9}$ were prepared following the same procedure. For the $\text{pIn}_{0.9}$ sample, a mixture containing the stoichiometric amounts of In_2O_3 , BiCl_3 , and AgCl was added to a flask containing HCl (37%) and heated up to 348 K under vigorous stirring for 15 min. After complete dissolution, 20 mmol L^{-1} of CsCl was added to the first solution, followed by heating to 383 K for 1 h and then allowing to cool to room temperature. The undoped perovskite microcrystals were washed with isopropyl alcohol, centrifuged, and dried overnight at 383 K. The samples $\text{pAg}_{0.6}\text{In}$ and $\text{pAg}_{0.6}\text{In}_{0.9}$ were synthesized following the same procedure and using the appropriate raw materials for the desired In-based perovskite compositions as described in Table 4. $\text{Yb}^{3+}/\text{Er}^{3+}$ co-doped In-based perovskite materials were prepared following the same procedure used for the undoped samples. Each of the three In-based perovskite hosts was obtained with a fixed concentration of Yb^{3+} in 10 mol% with varying the Er^{3+}

Table 3 Energy gap (ΔE), maximum relative thermal sensitivity (S_m), uncertainty in temperature (δT), and the temperature they occur at for different upconverting luminescent thermometers

Sample	ΔE (cm^{-1})	S_m (% K^{-1})	δT (K)	T_m (K)	Ref.
pAg _{0.6} In _{0.9} :Yb ³⁺ /Er ³⁺ (10:1)	752	1.3	0.3	293	This work
pAg _{0.6} In _{0.9} :Yb ³⁺ /Er ³⁺ (10:2)	753				
pAg _{0.6} In _{0.9} :Yb ³⁺ /Er ³⁺ (10:5)	752				
pAg _{0.6} In:Yb ³⁺ /Er ³⁺ (10:1)	752				
pAg _{0.6} In:Yb ³⁺ /Er ³⁺ (10:2)	752				
pAg _{0.6} In:Yb ³⁺ /Er ³⁺ (10:5)	752	1.2	0.3	298	32
pIn _{0.9} :Yb ³⁺ /Er ³⁺ (10:1)	752				
pIn _{0.9} :Yb ³⁺ /Er ³⁺ (10:2)	753				
pIn _{0.9} :Yb ³⁺ /Er ³⁺ (10:5)	753				
SrF ₂ :Yb ³⁺ /Er ³⁺ (20:2)	746				
KGd ₃ F ₁₀ :Yb ³⁺ /Er ³⁺ (20:5)	—	1.2	0.1	298	60
Y ₃ NbO ₇ :Yb ³⁺ /Er ³⁺ (1.5:0.5)	823	1.3	0.3	303	61
Y ₃ TaO ₇ :Yb ³⁺ /Er ³⁺ (29:0.6)	835	1.3	0.9	303	62
NaGdF ₄ :Yb ³⁺ /Er ³⁺ (20:2)	686	1.1	0.3	298	63

Table 4 Description of the chemical compositions of the In-based perovskite samples and corresponding labels used in this work

Chemical composition	Sample label
Cs ₂ AgIn _{0.9} Bi _{0.1} Cl ₆	pIn _{0.9}
Cs ₂ Ag _{0.6} Na _{0.4} InCl ₆	pAg _{0.6} In
Cs ₂ Ag _{0.6} Na _{0.4} In _{0.9} Bi _{0.1} Cl ₆	pAg _{0.6} In _{0.9}

amount from 1, 2, and 5 mol% in relation to the content of In, for a total of 9 co-doped samples with Yb³⁺:Er³⁺ ratios of 10:5, 10:2, and 10:1 for each In-based perovskite matrix.

X-Ray diffractometry

The powder X-ray diffraction (XRD) analysis of the polycrystalline In-based perovskite samples was carried out in a powder X-ray diffractometer equipped with a monochromator for Cu-K α (λ = 1.5418 Å) radiation (D8 Advance, Bruker). The measurements were performed at room temperature in the 2θ range from 10° to 60° at an angular rate of 0.5 s step⁻¹ and a scan step width of 0.02° using a position-sensitive detector (PSD, LynxEye, Bruker).

Raman spectroscopy

Raman scattering spectra were obtained in a Raman spectrometer coupled to a confocal microscope (LabRAM HR Evolution, Horiba) with a He-Ne laser (632.8 nm) excitation source. Data acquisition was performed by using the LabSpec 5 software (Horiba) in the spectral range of 10–400 cm⁻¹ with a scan step width of 0.8 cm⁻¹ using a 100× objective lens to focus on the samples.

Scanning electron microscopy

SEM micrographs were acquired in a scanning electron microscope (LEO 440, ZEISS) with a detector (7060, OXFORD) operating with an electron beam of 15 kV, 2.82 A current, and 200 pA probe I.

Diffuse reflectance spectroscopy

Diffuse reflectance spectroscopy (DRS) was performed in a UV–Vis–NIR spectrophotometer (UV 3600, Shimadzu) from 250 to

800 nm with a scan step width of 0.5 nm using barium sulfate (BaSO₄) as the standard.

Thermogravimetric analysis

Thermogravimetric analysis (TGA) was carried out in a simultaneous differential scanning calorimeter (SDT Q600, TA Instruments) from room temperature to 1000 °C at a heating rate of 10 °C min⁻¹ under a nitrogen atmosphere.

Photoluminescence spectroscopy and temperature-dependent measurements

The excitation and emission spectra of the Yb³⁺/Er³⁺ co-doped In-based perovskites were recorded in a Fluorolog 3 spectrofluorometer (FL3-22, Horiba) equipped with dual excitation and emission monochromators and photomultipliers for the visible (R928, Hamamatsu) and NIR (H10330-75, Hamamatsu) spectral ranges using the front face acquisition mode and a 450 W Xe arc lamp as the excitation source. Upconverting emission spectra were recorded using a 980 nm CW diode laser (DL980, CrystaLaser) as the excitation source. Temperature-dependent upconverting emission spectra of the samples were recorded in the 293–343 K temperature range using increments of 5 K. The samples were placed in a platinum crucible and heated in a temperature-controlled stage (T95-HT, LINKAM Scientific). The emission spectra were corrected by the instrument and obtained with an integration time of 150 ms and an increment of 0.5 nm for both excitation regimes.

Spectral deconvolution and energy gap determination

The emission spectra of the obtained In-based perovskites were analyzed by using a custom routine written in MATLAB 2022a under a license provided to the University of Aveiro. A polynomial baseline correction was applied to remove the electric noise from the spectrofluorometer signal, followed by the conversion of the emission spectrum from wavelength (nm) to energy (cm⁻¹) units using the Jacobian conversion.^{65,66} After that, 17 Gaussian functions were adjusted to the energy-converted emission spectra between the 17544–19608 cm⁻¹ spectral range. The peak energies were restricted to a ± 5 cm⁻¹ variation, the bounds of the widths were set between 40–180 cm⁻¹, and the lower bounds of the areas were set to zero to avoid negative values. The fits were considered well-adjusted when $r^2 > 0.99$. The barycenters of the emission bands arising in the green spectral range were computed as the averaged position of the Gaussian components corresponding to the ²H_{11/2} → ⁴I_{15/2} (eight Gaussian functions) and ⁴S_{3/2} → ⁴I_{15/2} (eight Gaussian functions) transitions of Er³⁺. The energy gap (ΔE) between the ²H_{11/2} and ⁴S_{3/2} emitting levels of Er³⁺ was then calculated from the difference between the barycenter of the ²H_{11/2} → ⁴I_{15/2} and ⁴S_{3/2} → ⁴I_{15/2} transitions (Fig. S5a in the ESI†). The Gaussian component peaking in the lower energy side was assigned to the ²H_{9/2} → ⁴I_{13/2} transition.

Thermometric analysis

The temperature-dependent upconverting emission spectra of the samples were analyzed by using a different MATLAB 2022a code.

After performing the baseline correction, the integrated emission of the $^2\text{H}_{11/2} \rightarrow ^4\text{I}_{15/2}$ ($I_{\text{H}} = 510\text{--}541\text{ nm}$) and $^4\text{S}_{3/2} \rightarrow ^4\text{I}_{15/2}$ ($I_{\text{S}} = 541\text{--}561\text{ nm}$) transitions were calculated by integrating the emission spectra, where the luminescence intensity ratio ($\Delta = I_{\text{H}}/I_{\text{S}}$) was computed for each temperature. The same approach was applied to the power-dependent emission spectra to determine the value of Δ in the no laser-induced heating regime (Δ_0 , i.e., the intercept of the Δ versus LPD plot, Figure S5b, ESI†).

Cell cultures and viability assay

A murine fibroblast L929 cell line was cultivated in Dulbecco's modified eagle's medium (DMEM, Sigma-Aldrich) with 10% fetal bovine serum (FBS, Sigma-Aldrich) and 1% penicillin-streptomycin at 37 °C in a humidified 5% CO₂ incubator for 24 h and then used to evaluate the cytotoxicity of the obtained perovskites by using the MTT colorimetric assay. First, 1×10^4 of the L929 cells were seeded in a 96 well plate (100 μL per well) and cultured overnight until total adhesion to the plate. Simultaneously, 12.0 mg mL⁻¹ of the undoped pIn_{0.9}, pAg_{0.6}In, and pAg_{0.6}In_{0.9} were prepared at a series of different concentrations (0.05, 0.10, and 0.20 mg mL⁻¹) and then 100 μL was added into each well and incubated for 48 h. Thereafter, 100 μL of 3-[4,5-dimethylthiazol-2-yl]-2,5-diphenyltetrazolium bromide (MTT, 1.00 mg mL⁻¹) reagent was added into each well and the cells were further incubated for 4 h. Finally, the supernatant was removed and 50 μL isopropanol was added into each well. Cell viability was obtained indirectly by measuring the MTT absorbance at 570 nm using a microplate spectrophotometer (SpectraMax ABS, Molecular Devices) and the viability values were calculated based on the absorbance of the control group (cells cultured without the addition of the perovskite samples).

Conflicts of interest

There are no conflicts to declare.

Acknowledgements

The authors acknowledge the financial support provided by the Brazilian research grants from São Paulo Research Foundation – FAPESP (2018/16126-7, 2021/08111-2, and 2019/18828-1), CAPES, and CNPq-Universal (424917/2018-1 and 405048/2021-1). F. E. M. acknowledges the funding received from the European Union's Horizon 2020 research and innovation programme under the Marie Skłodowska-Curie grant agreement no. 823941 (FUNGLASS) and the financial support from the Foundation for Science and Technology (FCT) through the Portuguese research grant UI/BD/151445/2021.

References

- 1 L. N. Quan, B. P. Rand, R. H. Friend, S. G. Mhaisalkar, T. W. Lee and E. H. Sargent, *Chem. Rev.*, 2019, **119**, 7444–7477.
- 2 M. Saliba, T. Matsui, J. Y. Seo, K. Domanski, J. P. Correa-Baena, M. K. Nazeeruddin, S. M. Zakeeruddin, W. Tress, A. Abate, A. Hagfeldt and M. Grätzel, *Energy Environ. Sci.*, 2016, **9**, 1989–1997.
- 3 K. Dave, M. H. Fang, Z. Bao, H. T. Fu and R. S. Liu, *Chem. – Asian J.*, 2020, **15**, 242–252.
- 4 Q. van Le, K. Hong, H. W. Jang and S. Y. Kim, *Adv. Electron. Mater.*, 2018, **4**, 1–28.
- 5 A. Babayigit, A. Ethirajan, M. Muller and B. Conings, *Nat. Mater.*, 2016, **15**, 247–251.
- 6 A. Babayigit, D. Duy Thanh, A. Ethirajan, J. Manca, M. Muller, H.-G. Boyen and B. Conings, *Sci. Rep.*, 2016, **6**, 18721.
- 7 M. Hauptman, R. Bruccoleri and A. D. Woolf, *Clin. Pediatr. Emerg. Med.*, 2017, **18**, 181–192.
- 8 M. R. Filip, S. Hillman, A. A. Haghighirad, H. J. Snaith and F. Giustino, *J. Phys. Chem. Lett.*, 2016, **7**, 2579–2585.
- 9 G. Volonakis, A. A. Haghighirad, R. L. Milot, W. H. Sio, M. R. Filip, B. Wenger, M. B. Johnston, L. M. Herz, H. J. Snaith and F. Giustino, *J. Phys. Chem. Lett.*, 2017, **8**, 772–778.
- 10 Y. Liu, A. Nag, L. Manna and Z. Xia, *Angew. Chem., Int. Ed.*, 2020, **60**(21), 11592–11603.
- 11 B. Yang, X. Mao, F. Hong, W. Meng, Y. Tang, X. Xia, S. Yang, W. Deng and K. Han, *J. Am. Chem. Soc.*, 2018, **140**, 17001–17006.
- 12 R. Chakraborty, P. K. Rajput, G. M. Anilkumar, S. Maqbool, R. Das, A. Rahman, P. Mandal and A. Nag, *J. Am. Chem. Soc.*, 2023, **145**(2), 1378–1388.
- 13 Y. Pei, D. Tu, C. Li, S. Han, Z. Xie, F. Wen, L. Wang and X. Chen, *Angew. Chem., Int. Ed.*, 2022, **61**(30), e202205276.
- 14 A. Zhang, Y. Liu, G. Liu and Z. Xia, *Chem. Mater.*, 2022, **34**, 3006–3012.
- 15 B. Nath, B. Pradhan and S. K. Panda, *New J. Chem.*, 2020, **44**, 18656–18661.
- 16 Y. Mahor, W. J. Mir and A. Nag, *J. Phys. Chem. C*, 2019, **123**, 15787–15793.
- 17 C. D. S. Brites, S. Balabhadra and L. D. Carlos, *Adv. Opt. Mater.*, 2019, **7**, 1–30.
- 18 J. C. Martins, A. R. N. Bastos, R. A. S. Ferreira, X. Wang, G. Chen and L. D. Carlos, *Adv. Photonics Res.*, 2021, **2**, 2000169.
- 19 T. Miyagawa, T. Fujie, Ferdinandus, T. T. Vo Doan, H. Sato and S. Takeoka, *ACS Appl. Mater. Interfaces*, 2016, **8**, 33377–33385.
- 20 S. Yu, D. Tu, W. Lian, J. Xu and X. Chen, *Sci. China Mater.*, 2019, **62**, 1071–1086.
- 21 Y. Shen, J. Lifante, E. Ximendes, H. D. A. Santos, D. Ruiz, B. H. Juárez, I. Zabala Gutiérrez, V. Torres Vera, J. Rubio Retama, E. Martín Rodríguez, D. H. Ortgies, D. Jaque, A. Benayas and B. del Rosal, *Nanoscale*, 2019, **11**, 19251–19264.
- 22 X. Zhu, W. Feng, J. Chang, Y.-W. Tan, J. Li, M. Chen, Y. Sun and F. Li, *Nat. Commun.*, 2016, **7**, 10437.
- 23 E. Carrasco, B. del Rosal, F. Sanz-Rodríguez, Á. J. de la Fuente, P. H. Gonzalez, U. Rocha, K. U. Kumar, C. Jacinto, J. G. Solé and D. Jaque, *Adv. Funct. Mater.*, 2015, **25**, 615–626.
- 24 D. Jaque and F. Vetrone, *Nanoscale*, 2012, **4**, 4301.

- 25 C. D. S. Brites, K. Fiaczyk, J. F. C. B. Ramalho, M. Sójka, L. D. Carlos and E. Zych, *Adv. Opt. Mater.*, 2018, **6**, 1701318.
- 26 I. E. Kolesnikov, A. A. Kalinichev, M. A. Kurochkin, E. V. Golyeva, E. Y. Kolesnikov, A. V. Kurochkin, E. Lähderanta and M. D. Mikhailov, *Sci. Rep.*, 2017, **7**, 18002.
- 27 R. G. Geitenbeek, H. W. de Wijn and A. Meijerink, *Phys. Rev. Appl.*, 2018, **10**, 064006.
- 28 T. P. Swieten, D. Yu, T. Yu, S. J. W. Vonk, M. Suta, Q. Zhang, A. Meijerink and F. T. Rabouw, *Adv. Opt. Mater.*, 2021, **9**, 2001518.
- 29 N.-N. Dong, M. Pedroni, F. Piccinelli, G. Conti, A. Sbarbati, J. E. Ramírez-Hernández, L. M. Maestro, M. C. Iglesias-de la Cruz, F. Sanz-Rodriguez, A. Juarranz, F. Chen, F. Vetrone, J. A. Capobianco, J. G. Solé, M. Bettinelli, D. Jaque and A. Speghini, *ACS Nano*, 2011, **5**, 8665–8671.
- 30 A. D. Pickel, A. Teitelboim, E. M. Chan, N. J. Borys, P. J. Schuck and C. Dames, *Nat. Commun.*, 2018, **9**, 4907.
- 31 P. Rühl, D. Wang, F. Garwe, R. Müller, M. Haase, K. W. Krämer, W. Paa, R. Heintzmann, S. H. Heinemann and H. Stafast, *J. Lumin.*, 2021, **232**, 117860.
- 32 S. Balabhadra, M. L. Debasu, C. D. S. Brites, R. A. S. Ferreira and L. D. Carlos, *J. Phys. Chem. C*, 2017, **121**, 13962–13968.
- 33 M. D. Dramićanin, *Methods Appl. Fluoresc.*, 2016, **4**, 042001.
- 34 T. J. Quinn, *Temperature*, Elsevier, 2nd edn, 1990.
- 35 A. M. P. Botas, C. D. S. Brites, J. Wu, U. Kortshagen, R. N. Pereira, L. D. Carlos and R. A. S. Ferreira, *Part. Part. Syst. Charact.*, 2016, **33**, 740–748.
- 36 J. F. C. B. Ramalho, S. F. H. Correia, L. Fu, L. L. F. António, C. D. S. Brites, P. S. André, R. A. S. Ferreira and L. D. Carlos, *Advanced Sci.*, 2019, **6**, 1900950.
- 37 K. M. N. de Souza, R. N. Silva, J. A. B. Silva, C. D. S. Brites, B. Francis, R. A. S. Ferreira, L. D. Carlos and R. L. Longo, *Adv. Opt. Mater.*, 2022, **10**, 2200770.
- 38 R. A. S. Ferreira, E. Mamontova, A. M. P. Botas, M. Shestakov, J. Vanacken, V. Moshchalkov, Y. Guari, L. F. Chibotaru, D. Luneau, P. S. André, J. Larionova, J. Long and L. D. Carlos, *Adv. Opt. Mater.*, 2021, **9**, 2101495.
- 39 N. M. Bhiri, M. Dammak, J. J. Carvajal, M. Aguiló, F. Díaz and M. C. Pujol, *J. Alloys Compd.*, 2022, **921**, 166020.
- 40 L. F. dos Santos, J. C. Martins, K. O. Lima, L. F. T. Gomes, M. T. de Melo, A. C. Tedesco, L. D. Carlos, R. A. S. Ferreira and R. R. Gonçalves, *Phys. B*, 2022, **624**, 413447.
- 41 M. Suta and A. Meijerink, *Adv. Theory Simul.*, 2020, **3**, 1–32.
- 42 E. Hemmer, A. Benayas, F. Légaré and F. Vetrone, *Nanoscale Horiz.*, 2016, **1**, 168–184.
- 43 H. Siddique, Z. Xu, X. Li, S. Saeed, W. Liang, X. Wang, C. Gao, R. Dai, Z. Wang and Z. Zhang, *J. Phys. Chem. Lett.*, 2020, **11**, 9572–9578.
- 44 M. B. Gray, J. D. Majher, T. A. Strom and P. M. Woodward, *Inorg. Chem.*, 2019, **58**, 13403–13410.
- 45 L. R. Morris and W. R. Robinson, *Acta Crystallogr., Sect. B: Struct. Sci.*, 1972, **28**, 653–654.
- 46 L. Zhang, Y. Fang, L. Sui, J. Yan, K. Wang, K. Yuan, W. L. Mao and B. Zou, *ACS Energy Lett.*, 2019, **4**, 2975–2982.
- 47 J. F. Suyver, J. Grimm, M. K. van Veen, D. Biner, K. W. Krämer and H. U. Güdel, *J. Lumin.*, 2006, **117**, 1–12.
- 48 G. Schaack and J. A. Koningstein, *J. Opt. Soc. Am.*, 1970, **60**, 1110.
- 49 G. Chai, G. Dong, J. Qiu, Q. Zhang and Z. Yang, *Sci. Rep.*, 2013, **3**, 1598.
- 50 P. Makuła, M. Pacia and W. Macyk, *J. Phys. Chem. Lett.*, 2018, **9**, 6814–6817.
- 51 W. Lee, S. Hong and S. Kim, *J. Phys. Chem. C*, 2019, **123**, 2665–2672.
- 52 D. Manna, T. K. Das and A. Yella, *Chem. Mater.*, 2019, **31**, 10063–10070.
- 53 W. J. Miniscalco, *J. Light Technol.*, 1991, **9**, 234–250.
- 54 J. Luo, X. Wang, S. Li, J. Liu, Y. Guo, G. Niu, L. Yao, Y. Fu, L. Gao, Q. Dong, C. Zhao, M. Leng, F. Ma, W. Liang, L. Wang, S. Jin, J. Han, L. Zhang, J. Etheridge, J. Wang, Y. Yan, E. H. Sargent and J. Tang, *Nature*, 2018, **563**, 541–545.
- 55 K. Zhu, Z. Wang, H. Xu and Z. Fu, *Adv. Opt. Mater.*, 2022, **10**, 2201182.
- 56 T. P. van Swieten, T. van Omme, D. J. van den Heuvel, S. J. W. Vonk, R. G. Spruit, F. Meirer, H. H. P. Garza, B. M. Weckhuysen, A. Meijerink, F. T. Rabouw and R. G. Geitenbeek, *ACS Appl. Nano Mater.*, 2021, **4**, 4208–4215.
- 57 F. Auzel, *Chem. Rev.*, 2004, **104**, 139–174.
- 58 F. Auzel, *J. Lumin.*, 1990, **45**, 341–345.
- 59 M. Pollnau, D. R. Gamelin, S. R. Lüthi, H. U. Güdel and M. P. Hehlen, *Phys. Rev. B: Condens. Matter Mater. Phys.*, 2000, **61**, 3337–3346.
- 60 K. de Oliveira Lima, L. F. dos Santos, R. Galvão, A. C. Tedesco, L. de Souza Menezes and R. R. Gonçalves, *Front. Chem.*, 2021, **9**, 712659.
- 61 F. H. Borges, J. C. Martins, F. J. Caixeta, L. D. Carlos, R. A. S. Ferreira and R. R. Gonçalves, *J. Lumin.*, 2022, **248**, 118986.
- 62 F. H. Borges, J. C. Martins, F. J. Caixeta, R. R. Pereira, L. D. Carlos, R. A. S. Ferreira and R. R. Gonçalves, *J. Solgel Sci. Technol.*, 2021, **102**, 249–263.
- 63 J. C. Martins, A. Skripka, C. D. S. Brites, A. Benayas, R. A. S. Ferreira, F. Vetrone and L. D. Carlos, *Front. Photon.*, 2022, **3**, DOI: [10.1007/s10971-021-05673-0](https://doi.org/10.1007/s10971-021-05673-0).
- 64 M. Kumar Chini, S. Goverapet Srinivasan, N. K. Tailor, Yukta, D. Salahub and S. Satapathi, *Chem. Phys.*, 2020, **529**, 110547.
- 65 J. Mooney and P. Kambhampati, *J. Phys. Chem. Lett.*, 2014, **5**, 3497.
- 66 J. Mooney and P. Kambhampati, *J. Phys. Chem. Lett.*, 2013, **4**, 3316–3318.